High Efficiency High Power Density Double-Clamp ZVS Flyback Converter With Secondary Absorption

Song Ding, Li Chen, Qinsong Qian, and Weifeng Sun, *Senior Member, IEEE*

***Abstract*—The double-clamp zero-voltage-switching (DCZVS) flyback converter can achieve high efficiency and high power density through high-frequency soft switching and inherent primary side regulation (PSR) feature. However, conventional resonance schemes for DCZVS flyback converters fail to simultaneously enable lossless leakage inductance energy recovery and high-precision PSR. In this article, a secondary absorption scheme is proposed for the DCZVS flyback converter, which employs the output capacitance of secondary-side synchronous rectifier switch to achieve lossless absorption of leakage inductance energy. Furthermore, the secondary absorption scheme reduces the voltage ripple of the clamp voltage and enhances PSR accuracy. The proposed scheme is validated on a 160–420 V input and 28 V/600 W output prototype. Compared with the highest power density level at present, the experimental prototype achieves a peak efficiency of 94.37% with an increase of 0.68% and achieves an ultra-high power density of 1290 W/inch^3 with an increase of 7.2%.**

***Index Terms*—Double-clamp zero-voltage-switching (DCZVS) flyback converter, high efficiency, high power density, primary side regulation (PSR), secondary absorption.**

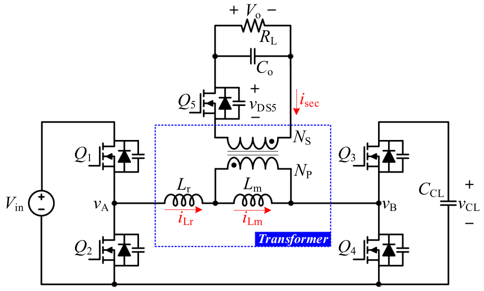

Fig. 1. Topology of the DCZVS flyback converter.

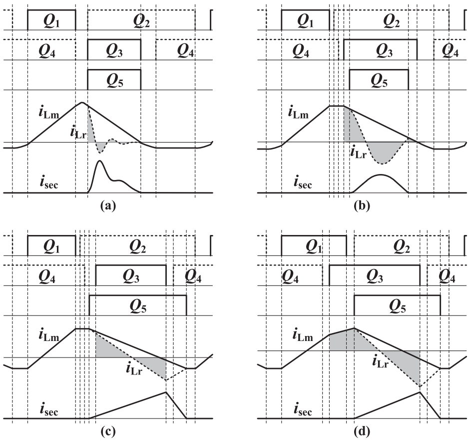

Fig. 2. Previous resonance schemes for DCZVS flyback converter. (a) Damping snubbing [8]. (b) Resonance absorption [9]. (c) Nonresonant [10]. (d) Nonresonant [11].

I. INTRODUCTION

THE rapid development of industries such as aerospace, electric vehicles, and industrial automation is forcing power converters to make breakthroughs toward wider input voltage range, higher efficiency, and higher power density [1], [2], [3]. Among numerous schemes for high power density converters with wide input range and galvanic isolation, the double-clamp zero-voltage-switching (DCZVS) flyback converter has emerged as a promising solution due to its high-frequency soft-switching and primary side regulation (PSR) characteristics [4], [5]. Fig. 1 shows the topology of the DCZVS flyback converter, which comprises four primary-side switches Q_1–Q_4, secondary-side synchronous rectifier (SR) switch Q_5, clamp capacitor C_{CL}, and a transformer. In this configuration, the leakage inductance serves as the resonant inductance, and resonates with clamp capacitor when the energy is transferred to the secondary side. Furthermore, the clamp voltage v_{CL} inherently correlates with the secondary-side output voltage, thereby facilitating PSR implementation without requiring the auxiliary winding typically used in conventional PSR architectures [6], [7].

Achieving high-frequency operation in the DCZVS flyback converter necessitates optimizing resonance parameters of leakage inductance L_r and clamp capacitor C_{CL} for proper current waveform, while maintaining soft switching through the negative current. Several resonance schemes have been proposed for DCZVS flyback converters in recent years [8], [10], [11]. As shown in Fig. 2(a), a damping snubbing scheme is proposed in [8]: the resonant frequency f_r of the L_r and C_{CL} is designed to be significantly higher than switching frequency f_S, and an extra damping resistor is used to dissipate the leakage inductance

---

Received 14 January 2025; revised 12 March 2025; accepted 27 March 2025. Date of publication 1 April 2025; date of current version 30 June 2025. This work was supported in part by the Programs of National Natural Science Foundation of China under Grant 62234005 and Grant 52177172, in part by Ministry of Education Joint Fund under Grant 8091B0204, and in part by National Key Research and Development Program under Grant 2023YFB3611905. Recommended for publication by Associate Editor A. Safaee. *(Corresponding author: Weifeng Sun.)*

The authors are with the National ASIC System Engineering Research Center, Southeast University, Nanjing 210096, China (e-mail: 230218146@seu.edu.cn; 230238432@seu.edu.cn; qianqinsong@seu.edu.cn; swffrog@seu.edu.cn).

Color versions of one or more figures in this article are available at https://doi.org/10.1109/TPEL.2025.3556253.

Digital Object Identifier 10.1109/TPEL.2025.3556253

energy during the resonance interval. Due to the high-frequency damped resonance, the resonant current i_{Lr} decays to zero during the energy transfer phase. After the clamp switch Q_3 turn OFF, the magnetizing inductance L_m of the transformer resonates with the output capacitance of switches Q_3 and Q_4 to form a negative current. This current magnitude is predictable by hardware parameters without requiring current sensing and remains independent of input voltage and load conditions. However, the leakage inductance energy is basically dissipated through the damping resistor, which decreases efficiency.

To achieve low-loss absorption of leakage inductance energy, a resonance absorption scheme is proposed in [9] as shown in Fig. 2(b): the resonant frequency of the leakage inductance and clamp capacitor is close to the switching frequency, and the leakage inductance energy is absorbed by the clamp capacitor during the energy transfer phase. Similarly, the negative current is generated through resonance process between the magnetizing inductance of the transformer and the output capacitance of switches Q_3 and Q_4. However, in this scheme, the resonant current is not fixed at the intersection point of the magnetizing current and resonant current. Consequently, negative current decreases as the output power increases, so the scheme suffers from an excessive negative current at light loads and an insufficient negative current at heavy loads.

As shown in Fig. 2(c), a nonresonant scheme in [10] also utilizes the clamp capacitor to absorb leakage inductance energy while significantly reducing the resonant frequency below switching frequency, thereby minimizing dependence on resonant parameters. However, this configuration requires direct negative current regulation through a current-sense resistor, which introduces additional parasitic losses.

As shown in Fig. 2(d), another nonresonant scheme has been proposed in [11], which similarly uses the clamp capacitor for leakage inductance energy absorption and implements ultra-low resonant frequency operation. In contrast to [10], this method calculates the negative current through the efficiency optimization algorithms rather than direct current sensing, while incorporating an additional operational phase when switches Q_1 and Q_3 conduct simultaneously to engage the clamp capacitor in the energy-storage process. However, there is still the problem of insufficient negative current and missing soft-switching at heavy load in this scheme.

More importantly, besides high-frequency soft-switching, high-precision PSR is crucial for DCZVS flyback converter to eliminate bulky isolation components such as optocouplers and achieve high power density [12], [13], [14]. In order to perform PSR through clamp voltage v_{CL} directly, the clamp capacitor C_{CL} needs to be small to minimize the sampling delay and to quickly reflect the change in output voltage [15]. Furthermore, the change rate ($\mathrm{d}i_{\mathrm{Lr}}/\mathrm{d}t$) of resonant current must be minimized at the end of the conduction of the clamp switch Q_3 to avoid the influence of the voltage across the leakage inductance on the sampling accuracy [7]. In addition, when switch Q_3 is ON, the integral of resonant current i_{Lr} (namely the shaded area in Fig. 2) corresponds to the voltage ripple of the clamp voltage. Consequently, among the four existing resonance schemes for DCZVS flyback converter, only the damping snubbing scheme is suitable for PSR, while the other three rely on secondary side regulation (SSR).

A comprehensive comparison of these resonance schemes is summarized in Table I. The damping snubbing scheme enables high-precision PSR, thereby supporting high power density, but incurs leakage inductance energy loss. In contrast, the remaining three schemes can achieve low-loss leakage inductance energy absorption via clamp capacitor, but the resultant clamp voltage is not suitable for PSR, ultimately constraining power density.

In this article, a secondary absorption scheme is proposed for DCZVS flyback converter, which offers three key advantages. First, the output capacitance of the secondary-side SR switch is harnessed to absorb the leakage inductance energy, thereby eliminating the need for a damping resistor and reducing associated loss. Second, the negative current is generated through the self-resonance between the output capacitance of switches and magnetizing inductance without current-sense. Negative current is independent of the load and input voltage. Third, compared with the damping snubbing scheme, the secondary absorption scheme further reduces the clamp voltage ripple, enabling high power density through high-precision PSR.

The rest of this article is organized as follows. In Section II, the operation principle of the DCZVS flyback converter with secondary absorption is described. Phenomenon, calculation method, and estimation by state trajectories of secondary absorption are discussed in detail in Section III. The conditions for soft-switching, as well as parameter design are analyzed in Section IV. Experimental results of a 600-W prototype are presented in Section V to illustrate the feasibility of the proposed secondary absorption scheme. Compared with the previous damping snubbing scheme, the prototype achieves a peak efficiency of 94.37% with an increase of 0.68%, and achieves an ultra-high power density of 1290 W/inch^3 with an increase of 7.2%. Finally, Section VI concludes this article.

II. OPERATING PRINCIPLE OF THE DCZVS FLYBACK CONVERTER WITH SECONDARY ABSORPTION

Fig. 3(a) illustrates the simulated waveforms of the DCZVS flyback converter in discontinuous current mode (DCM) with the proposed secondary absorption scheme. Each operating period consists of three main operating phases: energy-storage phase T_1, energy-transfer phase T_2, and freewheeling phase T_3. Considering the dead time between the three main phases, each operating period is divided into eight subintervals, wherein dead time T_{ZVS2} comprises three subintervals as switches Q_2, Q_5, and Q_3 undergo soft-switching turn-on successively. Fig. 4 illustrates the equivalent circuit of each subinterval, and Fig. 5 shows the simplified resonant model of each ZVS process. In Fig. 5, the output capacitance C_j of the secondary-side SR switch Q_5 is simplified as the primary-side capacitance C_{pj}, $C_{\mathrm{pj}} = C_{\mathrm{j}}/n^2$, the drain-source voltage v_{DS5} across C_{j} is translated as the primary voltage v_{pj}, $v_{\mathrm{pj}} = n{\cdot}v_{\mathrm{DS5}}$, and the secondary-side output capacitor C_{o} is approximated as the primary-side voltage source nV_{o}, where n is the turns ratio of primary and secondary windings of the transformer, $n = N_P/N_S$. The operating principle is demonstrated as follows.

TABLE I
COMPARISON OF SEVERAL RESONANCE SCHEMES FOR DCZVS FLYBACK CONVERTER

Scheme	Features	Pros	Cons
Damping snubbing [8]	- Leakage inductance energy is snubbed by damping - Negative current is generated through resonance process - $f_r \gg f_S$	- Suitable for PSR - Negative current is fixed without current-sense	- Leakage inductance energy is lost
Resonance absorption [9]	- Leakage inductance energy is absorbed by clamp capacitor - Resonance process generates the negative current - $f_r \approx f_S$	- High efficiency	- Negative current is not fixed and varies with load - Need current-sense - SSR control
Non-resonance absorption [10]	- Leakage inductance energy is absorbed by clamp capacitor - Negative current is regulated through current-sense directly - $f_r \ll f_S$	- High tolerance for hardware parameters	- Need current-sense - SSR control
Non-resonance absorption [11]	- Leakage inductance energy is absorbed by clamp capacitor - Negative current is calculated from the efficiency optimization - Clamp capacitor is involved in energy-storage - $f_r \ll f_S$	- High tolerance for hardware parameters - Without current-sense	- Lost ZVS at heavy load - SSR control
Secondary absorption (This Work)	- Leakage inductance energy is absorbed by secondary capacitance - Negative current is generated through resonance process - $f_r \gg f_S$	- Suitable for PSR - High efficiency - Negative current is fixed without current-sense	- Requires precise parameter design

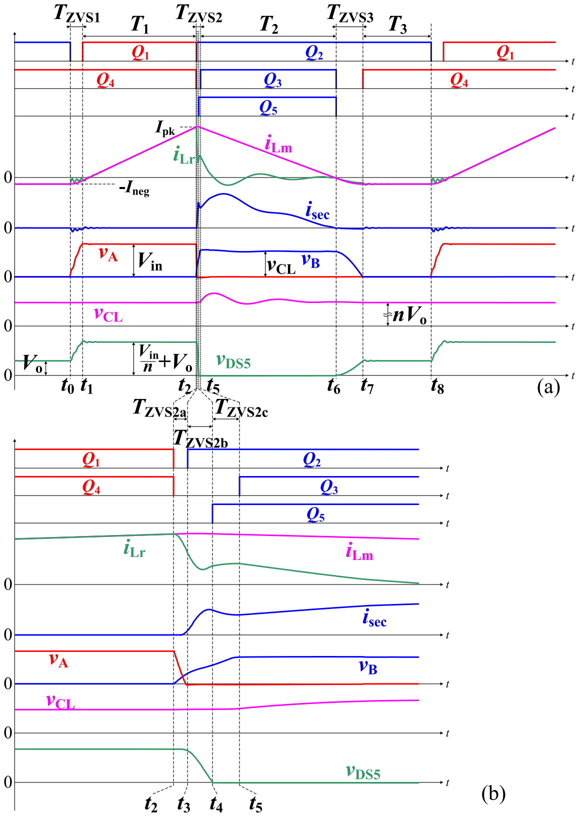

Fig. 3. Simulated waveforms of the DCZVS flyback converter with secondary absorption scheme. (a) Overall review. (b) Zoom-in review of T_{ZVS2}.

Interval T_{ZVS1} [t_0, t_1] [Figs. 4(a) and 5(a)]: Prior to t_0, switches Q_2 and Q_4 conduct to clamp the negative freewheeling current -I_{neg} in the magnetizing inductance L_m. At t_0, switch Q_2 is turned OFF, and magnetizing inductance L_m resonates with the capacitance C_A at point A and the junction capacitance C_{pj}. From Fig. 3, the leakage inductance can be negligible to magnetizing current i_{Lm}, voltage v_A and voltage v_{pj} during T_{ZVS1}

$$i_{Lm}(t) = \frac{C_1}{C_A} \cdot i_{Lr}(t) = -I_{neg} \cos \omega_1 (t - t_0) \tag{1}$$

$$v_A(t) = I_{neg} Z_1 \sin \omega_1 (t - t_0) \tag{2}$$

$$v_{pj}(t) = nV_o + I_{neg} Z_1 \sin \omega_1 (t - t_0) \tag{3}$$

where capacitance C_A consists of the output capacitance of switches Q_1 and Q_2, $C_A = C_{OSS1} + C_{OSS2}$, and $C_1 = C_A + C_{pj}$, $\omega_1 = \frac{1}{\sqrt{L_m C_1}}$, $Z_1 = \sqrt{L_m/C_1}$. When voltage v_A rises from zero to input voltage V_{in}, this ZVS phase ends.

Interval T_1 [t_1, t_2] [Fig. 4(b)]: At t_1, v_A rises to V_{in}, C_A is fully charged and thus switch Q_1 achieves ZVS conduction. The magnetizing inductance L_m stores energy from the input source V_{in} and magnetizing current i_{Lm} increases linearly, switches Q_1 and Q_4 are turned OFF at t_2 simultaneously and the energy storage phase ends. Denote the magnetizing current $i_{Lm}(t_2)$ and the resonance current $i_{Lr}(t_2)$ at t_2 as the peak current I_{pk}.

Interval T_{ZVS2a} [t_2, t_3] [Figs. 4(c) and 5(b)]: The output capacitances of all switches collectively form a high-order resonant network with the inductance L_m and L_r. However, as shown in Fig. 3(b), the magnetizing current i_{Lm} remains nearly constant at I_{pk} throughout the entire T_{ZVS2} subintervals. This allows L_m to be approximated as a constant current source in the equivalent circuits of Fig. 5(b) and (c). As the secondary-side junction capacitance C_j is involved in the resonance, resonant current i_{Lr} dips rapidly, and the leakage inductance energy is absorbed by C_j. The resonant current i_{Lr}, voltage v_A, voltage v_B and voltage v_{pj} during T_{ZVS2a} are expressed as follows:

$$i_{Lr}(t) = I_{pk} \left[\frac{C_{2a}}{C_{pj}} + \left(1 - \frac{C_{2a}}{C_{pj}}\right) \cos \omega_{2a} (t - t_2) \right] \tag{4}$$

$$\begin{aligned} v_A(t) = V_{in} - \frac{I_{pk}}{C_A} \Bigg[& \frac{C_{2a}}{C_{pj}} (t - t_2) \\ & + \left(1 - \frac{C_{2a}}{C_{pj}}\right) \frac{\sin \omega_{2a} (t - t_2)}{\omega_{2a}} \Bigg] \end{aligned} \tag{5}$$

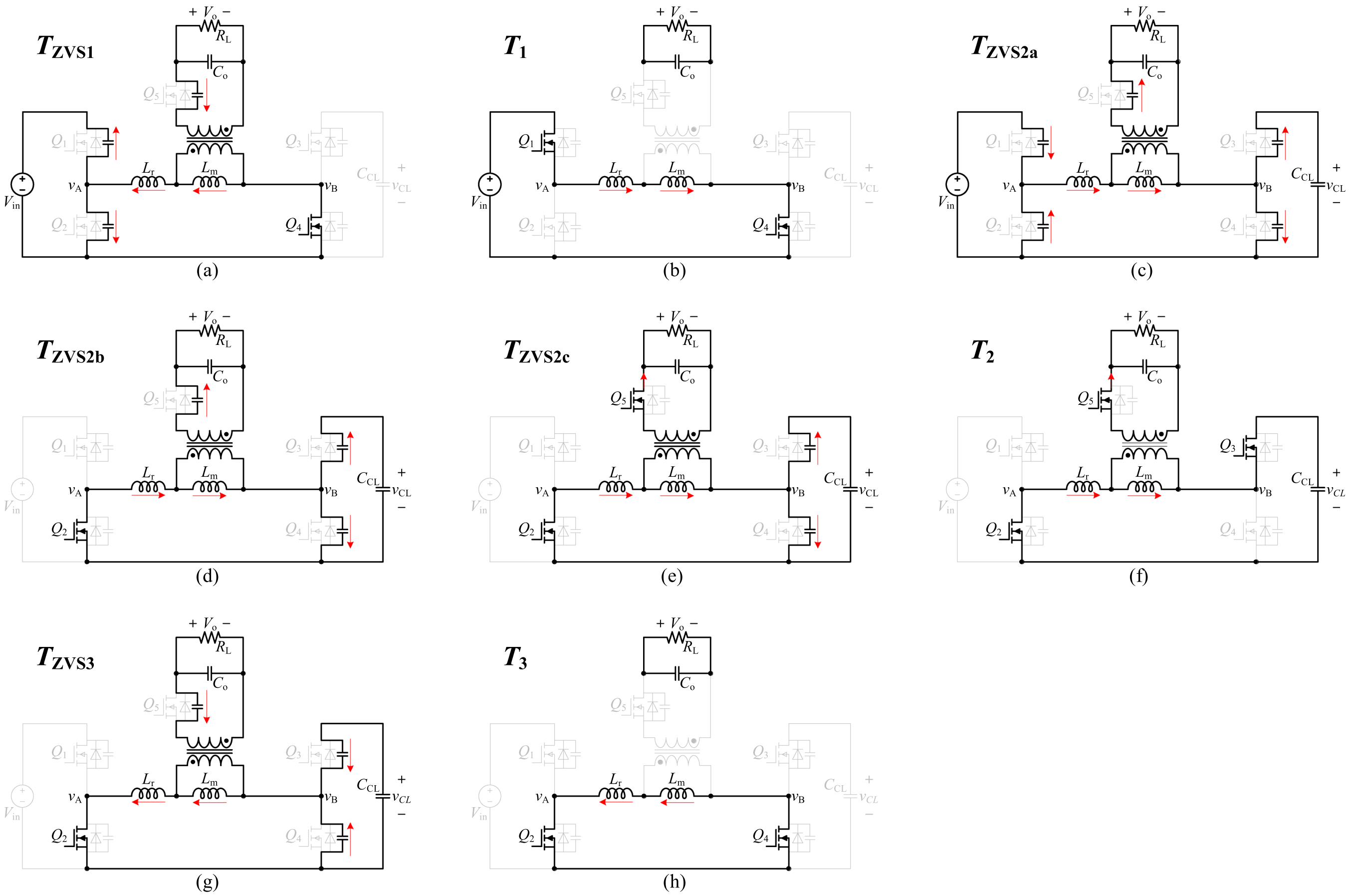

Fig. 4. Equivalent circuits. (a) T_{ZVS1} $[t_0, t_1]$. (b) T_1 $[t_1, t_2]$. (c) $T_{\mathrm{ZVS2}a}$ $[t_2, t_3]$. (d) $T_{\mathrm{ZVS2}b}$ $[t_3, t_4]$. (e) $T_{\mathrm{ZVS2}c}$ $[t_4, t_5]$. (f) T_2 $[t_5, t_6]$. (g) T_{ZVS3} $[t_6, t_7]$. (h) T_3 $[t_7 - t_8]$.

$$v_B(t) = \frac{I_{\mathrm{pk}}}{C_B}\left[\frac{C_{2a}}{C_{\mathrm{pj}}}(t-t_2) + \left(1-\frac{C_{2a}}{C_{\mathrm{pj}}}\right)\frac{\sin\omega_{2a}(t-t_2)}{\omega_{2a}}\right] \tag{6}$$

$$v_{\mathrm{pj}}(t) = V_{\mathrm{in}} + nV_o - \frac{I_{\mathrm{pk}}}{C_{\mathrm{pj}}}\left(1-\frac{C_{2a}}{C_{\mathrm{pj}}}\right)\left[t-t_2-\frac{\sin\omega_{2a}(t-t_2)}{\omega_{2a}}\right] \tag{7}$$

where capacitance C_B mainly consists of the output capacitance of switches Q_3 and Q_4, $C_B \approx C_{\mathrm{OSS3}} + C_{\mathrm{OSS4}}$, and $\omega_{2a} = \frac{1}{\sqrt{L_r C_{2a}}}$, $\frac{1}{C_{2a}} = \frac{1}{C_A} + \frac{1}{C_B} + \frac{1}{C_{\mathrm{pj}}}$.

At t_3, voltage v_A decreases to zero, so the body diode of switch Q_2 conducts.

Interval $T_{\mathrm{ZVS2}b}$ $[t_3, t_4]$ [Figs. 4(d) and 5(c)]: Body diode of switch Q_2 remains ON, and resonant inductance L_r resonates with capacitance C_b and C_{pj}, so voltage v_{pj} continues to decrease. The resonant current i_{Lr}, voltage v_B and v_{pj} can be derived as follows:

$$i_{\mathrm{Lr}}(t) = i_{\mathrm{Lr}}(t_3)\cos\omega_{2b}(t-t_3) + \frac{v_{t3}}{Z_{2b}}\sin\omega_{2b}(t-t_3) + I_{\mathrm{pk}}\frac{C_{2b}}{C_{\mathrm{pj}}}\cdot[1-\cos\omega_{2b}(t-t_3)] \tag{8}$$

$$v_B(t) = v_B(t_3) + \frac{i_{\mathrm{Lr}}(t_3) - I_{\mathrm{pk}}\cdot\frac{C_{2b}}{C_{\mathrm{pj}}}}{C_B}\cdot\frac{\sin\omega_{2b}(t-t_3)}{\omega_{2b}} + \frac{v_{t3}}{C_B Z_{2b}}\cdot\frac{1-\cos\omega_{2b}(t-t_3)}{\omega_{2b}} + \frac{I_{\mathrm{pk}}}{C_B + C_{\mathrm{pj}}}\cdot(t-t_3) \tag{9}$$

$$v_{\mathrm{pj}}(t) = v_{\mathrm{pj}}(t_3) + \frac{i_{\mathrm{Lr}}(t_3) - I_{\mathrm{pk}}\cdot\frac{C_{2b}}{C_{\mathrm{pj}}}}{C_{\mathrm{pj}}}\cdot\frac{\sin\omega_{2b}(t-t_3)}{\omega_{2b}} + \frac{v_{t3}}{C_{\mathrm{pj}} Z_{2b}}\cdot\frac{1-\cos\omega_{2b}(t-t_3)}{\omega_{2b}} - \frac{I_{\mathrm{pk}}}{C_B + C_{\mathrm{pj}}}(t-t_3) \tag{10}$$

where $\frac{1}{C_{2b}} = \frac{1}{C_B} + \frac{1}{C_{\mathrm{pj}}}$, $\omega_{2b} = \frac{1}{\sqrt{L_r C_{2b}}}$, $Z_{2b} = \sqrt{L_r / C_{2b}}$, $v_{t3} = nV_o - v_{\mathrm{pj}}(t_3) - v_B(t_3)$, and $i_{Lr}(t_3)$, $v_{\mathrm{pj}}(t_3)$, and $v_B(t_3)$ are the current $\mathrm{i_{Lr}}$, voltage $\mathrm{v_{pj}}$ and voltage v_B at t_3 respectively.

At t_4, voltage v_{pj} decreases to zero, and SR switch Q_5 achieves ZVS turn-ON.

Interval $T_{\mathrm{ZVS2}c}$ $[t_4, t_5]$ [Figs. 4(e) and 5(d)]: Because of the conduction of switch Q_5, the secondary-side output voltage V_o is reflected across the magnetizing inductance L_m, so inductance L_r resonates in series with capacitance C_B and the voltage v_B continues to rise. The resonant current i_{Lr} and voltage v_B are

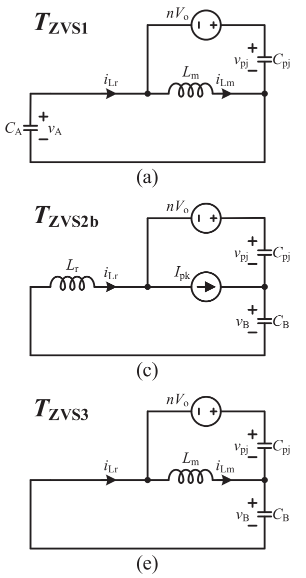

Fig. 5. Simplified ZVS model. (a) T_{ZVS1} [t_0, t_1]. (b) $T_{\mathrm{ZVS2}a}$ [t_2, t_3]. (c) $T_{\mathrm{ZVS2}b}$ [t_3, t_4]. (d) $T_{\mathrm{ZVS2}c}$ [t_4, t_5]. (e) T_{ZVS3} [t_6, t_7].

expressed in (11) and (12), respectively

$$i_{\mathrm{Lr}}(t) = i_{\mathrm{Lr}}(t_4)\cos\omega_{2c}(t-t_4) + \frac{v_{t4}}{Z_{2c}}\sin\omega_{2c}(t-t_4) \tag{11}$$

$$v_B(t) = i_{\mathrm{Lr}}(t_4)Z_{2c}\sin\omega_{2c}(t-t_4) + nV_{\mathrm{o}} - v_{t4}\cos\omega_{2c}(t-t_4) \tag{12}$$

where $\omega_{2c} = \frac{1}{\sqrt{L_r C_B}}$, $v_{t4} = nV_{\mathrm{o}} - v_B(t_4)$, $Z_{2c} = \sqrt{L_r/C_B}$ and $i_{\mathrm{Lr}}(t_4)$ and $v_B(t_4)$ are the current i_{Lr} and voltage v_B at t_4.

At t_5, voltage v_B rises to the clamp voltage v_{CL} (about nV_{o}), so that Q_3 can achieve soft-switching conduction.

Interval T_2 [t_5, t_6] [Fig. 4(f)]: At t_5, switches Q_2, Q_3, and Q_5 all realize ZVS conduction, so the energy stored in magnetizing inductance is transferred to the secondary side, and magnetizing current i_{Lm} decreases linearly. The resonant inductance L_r resonates with the clamp capacitor C_{CL} at high frequency, and the resonant current i_{Lr} gradually decays to zero under the damping effect of the on-resistance. The magnetizing current i_{Lm}, resonant current i_{Lr} and clamp voltage v_{CL} are given by

$$i_{\mathrm{Lm}}(t) = I_{\mathrm{pk}} - \frac{nV_{\mathrm{o}}}{L_{\mathrm{m}}}\cdot(t-t_5) \tag{13}$$

$$i_{\mathrm{Lr}}(t) = -\frac{\alpha\cdot L_r}{Z_r}\cdot i_{\mathrm{Lr}}(t_5)\,e^{-\alpha(t-t_5)}\sin\omega_r(t-t_5) + i_{\mathrm{Lr}}(t_5)\,e^{-\alpha(t-t_5)}\cos\omega_r(t-t_5) \tag{14}$$

$$v_{\mathrm{CL}}(t) = nV_{\mathrm{o}} + \frac{i_{\mathrm{Lr}}(t_5)}{C_{\mathrm{CL}}\omega_r}\cdot e^{-\alpha(t-t_5)}\sin\omega_r(t-t_5) \tag{15}$$

where α is the damping coefficient, $\alpha = \frac{R_2+R_3+\mathrm{n}^2\cdot R_5}{2\cdot L_r}$, and R_2, R_3, and R_5 are the on-resistance of switches Q_2, Q_3, and Q_5; the angular frequency $\omega_r = \sqrt{(L_r/C_{\mathrm{CL}})^2 - \alpha^2} > 0$, and resonant period $T_r = 2\pi/\omega_r$ is far briefer than the energy transfer phase T_2; and $i_{\mathrm{Lr}}(t_5)$ are the current i_{Lr} at t_5.

At t_6, magnetizing current i_{Lm} decreases to the resonant current i_{Lr}, so the secondary current i_{sec} also decreases to 0, and the energy transfer phase ends.

Interval T_{ZVS3} [t_6, t_7] [Figs. 4(g) and 5(e)]: At t_6, both the magnetizing current i_{Lm} and resonant current i_{Lr} are nearly zero, and switches Q_3 and Q_5 realize ZCS turn-OFF. Then, the magnetizing inductance L_m resonates with capacitance C_B and C_{pj}, so voltage v_B decreases from the clamp voltage v_{CL} and magnetizing current i_{Lm} grows negatively from zero. Neglecting the effect of leakage inductance L_r, the magnetizing current i_{Lm}, voltage v_B and voltage v_{CL} are expressed as follows:

$$i_{\mathrm{Lm}}(t) = \frac{C_3}{C_B}\cdot i_{\mathrm{Lr}}(t) = -\frac{nV_{\mathrm{o}}}{Z_3}\sin\omega_3(t-t_6) \tag{16}$$

$$v_B(t) = nV_{\mathrm{o}}\cos\omega_3(t-t_6) \tag{17}$$

$$v_{\mathrm{pj}}(t) = nV_{\mathrm{o}} - nV_{\mathrm{o}}\cos\omega_3(t-t_6) \tag{18}$$

where $C_3 = C_B + C_{\mathrm{pj}}$, $Z_3 = \sqrt{L_m/C_3}$, $\omega_3 = \frac{1}{\sqrt{L_m C_3}}$.

At t_7, voltage v_B decreases to zero, so switch Q_4 can be turned ON with ZVS. And the negative magnetizing current i_{Lm} at t_7 is

$$i_{\mathrm{Lm}}(t_7) = -I_{\mathrm{neg}} = -\frac{nV_{\mathrm{o}}}{Z_3}. \tag{19}$$

Interval T_3 [t_7, t_8] [Fig. 4(h)]: Due to the conduction of switch Q_2 and Q_4, the negative current -I_{neg} is freewheeling in the magnetizing inductance L_m and will be used for the soft-switching of switching Q_1 in the next period. When switch Q_2 is turned OFF at t_8, the next period starts.

It should be noted that, the DCZVS flyback converter may go from DCM to critical current mode (CrCM) at heavy load. In CrCM, this subinterval T_3 is brief or even disappear.

Besides, substituting $v_A = V_{\mathrm{in}}$ into (2) and $v_B = 0$ into (17), dead-time T_{ZVS1} and T_{ZVS3} can be expressed in (20) and (21). The dead time T_{ZVS2} will be analyzed in detail in Section III

$$T_{\mathrm{ZVS1}} = \arcsin\left(\frac{V_{in}}{nV_{\mathrm{o}}}\sqrt{\frac{C_1}{C_3}}\right)\cdot\sqrt{L_m C_1} \tag{20}$$

$$T_{\mathrm{ZVS3}} = \frac{1}{4}\cdot\frac{2\pi}{\omega_3} = \frac{\pi}{2}\cdot\sqrt{L_m C_3}. \tag{21}$$

III. SECONDARY ABSORPTION CONSIDERATIONS

A. *Secondary Absorption Caused by Capacitance C_j*

As observed in Fig. 3(b), resonant current i_{Lr} exhibits an abrupt dip during subinterval $T_{\mathrm{ZVS2}a}$, analogous to the current dip phenomenon in active clamp flyback converter in [16]. This mechanism ensures that partial leakage inductance energy is absorbed by the secondary-side capacitance C_j during T_{ZVS2}, with the recovered energy facilitating the negative current generation during T_{ZVS3}. Consequently, this secondary-absorption process prevents the complete dissipation of leakage inductance energy through damping components. As defined in (22), the recovery factor κ_{rec} quantifies the proportion of recovered leakage inductance energy relative to the total leakage

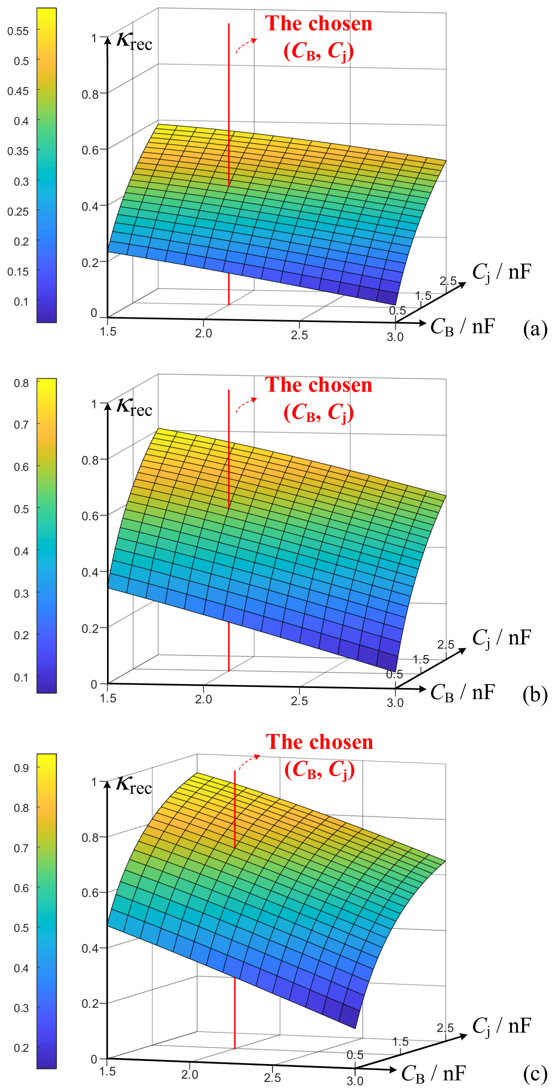

Fig. 6. Curves of $\kappa_{\rm rec}$ as function of C_B and C_j at full load. (a) $V_{\rm in}$=160 V, $I_{\rm pk}$=16 A. (b) $V_{\rm in}$=280 V, $I_{\rm pk}$=13 A. (b) $V_{\rm in}$=420 V, $I_{\rm pk}$=12 A.

TABLE II
KEY PARAMETERS FOR THE PROTOTYPE

Parameter	Value	Parameter in sub-cell	Value
Input voltage $V_{\rm in}$	160–420 V	Turns ratio $n_{\rm eq}$	3
Output voltage $V_{\rm o}$	28 V	Inductance $L_{\rm m,eq}$	4.8 μH
Output power	0–600 W	Inductance $L_{\rm r,eq}$	≈ 200 nH
Output Capacitor $C_{\rm o}$	1000 μF	Capacitance $C_{\rm CL}$	22 nF
Switching frequency $f_{\rm S}$	65–710 kHz	Capacitance $C_{\rm A}$	156 pF
Size	46*23*7.2 mm^3	Capacitance $C_{\rm B}$	2 nF
Power density	1290 W/inch^3	Capacitance $C_{\rm j}$	1.5 nF

inductance energy

$$\kappa_{\rm rec} = 1 - \frac{i_{\rm Lr}^2(t_5)}{I_{\rm pk}^2} = f\left(C_A, C_B, C_j, n, L_r, V_{\rm in}, V_{\rm o}, I_{\rm pk}\right). \tag{22}$$

Fig. 6 shows the curves of $\kappa_{\rm rec}$ as function of C_B and C_j at full load and different voltage with the parameters listed in Table II.

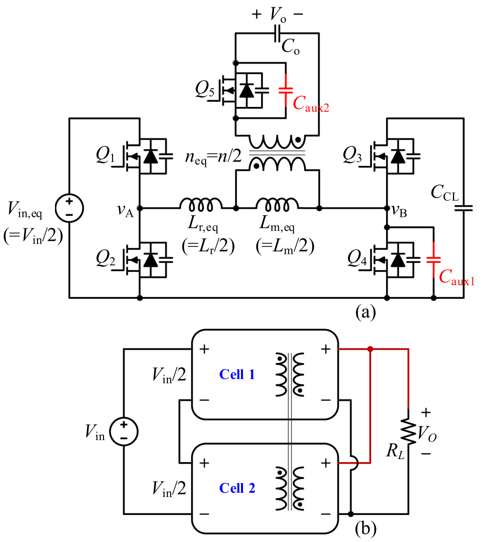

Fig. 7. Dual-cell ISOP structure for DCZVS flyback converter. (a) Schematics of subcells in a cell converter. (b) Simplified structure block of cells.

According to (20) and (21), dead time of the DCZVS flyback converter exhibits a positive correlation with the magnetizing inductance L_m. As identified in [5], dead time is also a critical limitation for power density improvement. Consequently, prototype in this article retains the dual-cell transformer-coupled input-series-output-parallel (ISOP) structure in [5], which effectively minimizes dead time while optimizing power density, as shown in Fig. 7(b). In each subcell, equivalent input voltage $V_{\rm in,eq}$, equivalent magnetizing inductance $L_{m,\rm eq}$, equivalent resonant inductance $L_{r,\rm eq}$ and equivalent turns ratio $n_{\rm eq}$ are half of those of the whole converter. Fig. 7(a) shows the capacitance adjustment action that two external auxiliary capacitors $C_{\rm aux1}$ and $C_{\rm aux2}$ are connected in parallel across switches Q_3 and Q_5, modifying C_B and C_j to enhance secondary absorption.

B. Calculation of Recovery Factor κ_{rec}

The $\kappa_{\rm rec}$ is dependent on both hardware parameters (C_A, C_B, C_j, n, L_r) and operating conditions ($V_{\rm in}$, $V_{\rm o}$, $I_{\rm pk}$). More complex than the calculation of the dip current in [16], the $\kappa_{\rm rec}$ in the DCZVS converter needs to be calculated step-by-step based on the three different resonant subintervals included in $T_{\rm ZVS2}$.

$T_{{\rm ZVS2}a}$ can be obtained by s substituting $v_A\ (t_3) =\ 0$ into (5). The transcendental equation for $T_{{\rm ZVS2}a}$ is expressed as

$$\frac{C_{2a}}{C_{\rm pj}} \cdot T_{{\rm ZVS2}a} + \left(1 - \frac{C_{2a}}{C_{\rm pj}}\right) \frac{\sin \omega_{2a} T_{{\rm ZVS2}a}}{\omega_{2a}} = \frac{V_{\rm in} C_A}{I_{\rm pk}}. \tag{23}$$

Then substituting (23) into (4), (6), and (7), current $i_{\rm Lr}$, voltage v_B and voltage $v_{\rm pj}$ at t_3 can be derived as follows:

$$i_{\rm Lr}\left(t_3\right) = I_{\rm pk}\left[\frac{C_{2a}}{C_{\rm pj}} + \left(1 - \frac{C_{2a}}{C_{\rm pj}}\right)\cos \omega_{2a} T_{{\rm ZVS2}a}\right] \tag{24}$$

$$v_B\left(t_3\right) = \frac{C_A}{C_B} V_{\rm in} \in \left(0, nV_{\rm o}\right) \tag{25}$$

$$v_{\rm pj}\left(t_3\right) = V_{\rm in} + nV_{\rm o} - \frac{I_{pk} T_{{\rm ZVS2}a} - C_A V_{\rm in}}{C_{\rm pj}} \in \left(0, V_{\rm in} + nV_{\rm o}\right). \tag{26}$$

Besides, $v_B(t_3) < nV_{\rm o}$ and $v_{\rm pj}(t_3) > 0$.

Moreover, by substituting $v_{\rm pj}\,(t_4) = 0$ into (10), $T_{{\rm ZVS}2b}$ can be solved from the following transcendental equation:

$$\left(1-\frac{C_{2b}}{C_{\rm pj}}\right)\cdot T_{{\rm ZVS}2b}-\left(\frac{i_{\rm Lr}\,(t_3)}{I_{\rm pk}}-\frac{C_{2b}}{C_{\rm pj}}\right)\cdot\frac{\sin\omega_{2b}T_{{\rm ZVS}2b}}{\omega_{2b}} - \frac{v_{t3}}{I_{\rm pk}Z_{2b}}\cdot\frac{1-\cos\omega_{2b}T_{{\rm ZVS}2b}}{\omega_{2b}}=\frac{v_{\rm pj}\,(t_3)\,C_{\rm pj}}{I_{\rm pk}} \tag{27}$$

where

$$v_{t3} = nV_{\rm o} - v_{\rm pj}\,(t_3) - v_B\,\,(t_3) = \frac{I_{\rm pk}T_{{\rm ZVS}2a}}{C_{\rm pj}} - \frac{C_AV_{\rm in}}{C_{2a}}. \tag{28}$$

Substituting (27) into (8) and (9), current $i_{\rm Lr}$ and voltage v_B at t_4 can be obtained as follows and $v_B(t_4) < nV_{\rm o}$:

$$i_{\rm Lr}\,(t_4) = i_{\rm Lr}\,\,(t_3)\cos\omega_{2b}T_{{\rm ZVS}2b} + \frac{v_{t3}}{Z_{2b}}\sin\omega_{2b}T_{{\rm ZVS}2b} + I_{\rm pk}\frac{C_{2b}}{C_{\rm pj}}\cdot(1-\cos\omega_{2b}T_{{\rm ZVS}2b}) \tag{29}$$

$$v_B\,(t_4) = \frac{I_{\rm pk}\,(T_{{\rm ZVS}2a}+T_{{\rm ZVS}2b}) - C_{\rm pj}\,(V_{\rm in}+nV_{\rm o})}{C_B} \times \in (0, nV_{\rm o}\,). \tag{30}$$

Furthermore, according to (11) and (12), the trajectory equation of current $i_{\rm Lr}$ and voltage v_B during $T_{{\rm ZVS}2c}$ is given by

$$L_r\cdot i^2_{\rm Lr}\,(t) + C_B\cdot\,\,[v_B\,(t) - nV_{\rm o}]^2 = L_r\,\,\cdot i^2_{\rm Lr}\,(t_4) + C_B\cdot[v_B\,(t_4) - nV_{\rm o}]^2. \tag{31}$$

Substituting $v_B\,(t_5) = nV_{\rm o}$ into (31), current $i_{\rm Lr}$ at t_5 can be obtained:

$$i^2_{\rm Lr}\,\,(t_5) = i^2_{\rm Lr}\,\,(t_4) + \frac{C_B}{L_r}\cdot[v_B\,(t_4) - nV_{\rm o}]^2. \tag{32}$$

Finally, recovery factor $\kappa_{\rm rec}$ can be solved by combining (23)–(32)

$$\kappa_{\rm rec} = 1 - \frac{C_B}{L_r}\left(\frac{T_{{\rm ZVS}2a}+T_{{\rm ZVS}2b}}{C_B} - \frac{C_{\rm pj}\,(V_{\rm in}+nV_{\rm o})}{I_{\rm pk}C_B} - \frac{nV_{\rm o}}{I_{\rm pk}}\right)^2 - \left(m_1\cos\omega_{2b}T_{{\rm ZVS}2b} + m_2\sin\omega_{2b}T_{{\rm ZVS}2b} + \frac{C_{2b}}{C_{\rm pj}}\right)^2 \tag{33}$$

where

$$\begin{cases} m_1 = \frac{C_{2a}-C_{2b}}{C_{\rm pj}} + \left(1-\frac{C_{2a}}{C_{\rm pj}}\right)\cos\omega_{2a}T_{{\rm ZVS}2a} \\ m_2 = \frac{T_{{\rm ZVS}2a}}{C_{\rm pj}Z_{2b}} - \frac{(C_A+C_{2b})V_{\rm in}}{C_{2b}Z_{2b}I_{\rm pk}} \end{cases}. \tag{34}$$

Fig. 8 presents the recovery factor $\kappa_{\rm rec}$ calculated according to (33) with the hardware parameters in Table II. Although recovery factor $\kappa_{\rm rec}$ can be calculated quantitatively according to (33), transcendental nature of (23) and (27) impedes direct application for hardware parameter design and minimum peak current determination. Subsequent analysis, therefore employs the state-trajectory method to examine the three resonant subintervals in the $T_{\rm ZVS2}$ phase [17], [18], thereby enabling estimation of the recovery factor $\kappa_{\rm rec}$.

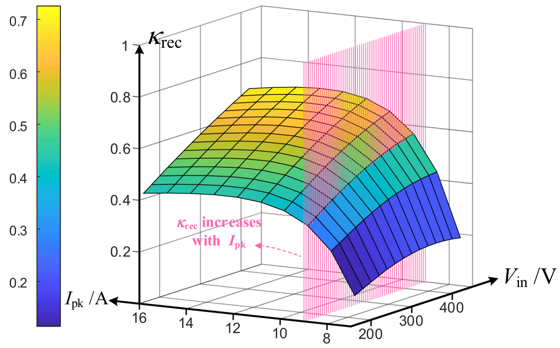

Fig. 8. Recovery factor $\kappa_{\rm rec}$ at different operating conditions.

C. State Trajectories in the T_{ZVS2}

According to Fig. 5(b), state equation of $i_{\rm Lr}$, v_A, v_B, and $v_{\rm pj}$ in $T_{{\rm ZVS}2a}$ phase is

$$\begin{cases} L_r\frac{d}{dt}i_{\rm Lr} = -\,(v_B + v_{\rm pj} - nV_{\rm o} - v_A) \\ C_A\frac{d}{dt}v_A = -i_{\rm Lr} \\ C_B\frac{d}{dt}v_B = i_{\rm Lr} \\ C_{\rm pj}\frac{d}{dt}v_{\rm pj} = i_{\rm Lr} - I_{\rm pk} \end{cases}. \tag{35}$$

From (35), the state equation of $T_{{\rm ZVS}2a}$ phase is simplified as

$$\frac{di_{\rm Lr}}{d\,(v_A - v_B - v_{\rm pj})} = \frac{C_{2a}}{L_r}\cdot\frac{v_A - v_B - v_{\rm pj} + nV_{\rm o}}{-i_{\rm Lr}\,(t) + \frac{C_{2a}}{C_{\rm pj}}I_{\rm pk}}. \tag{36}$$

Then, the state trajectory of $T_{{\rm ZVS}2a}$ phase is

$$\left(\frac{i_{\rm Lr}}{I_{\rm pk}} - \frac{C_{2a}}{C_{\rm pj}}\right)^2 + \frac{C_{2a}}{L_rI^2_{\rm pk}}(v_A - v_B - v_{\rm pj} + nV_{\rm o})^2 = \left(1 - \frac{C_{2a}}{C_{\rm pj}}\right)^2 \tag{37}$$

which means that v_A-v_B-$v_{\rm pj}$ and $i_{\rm Lr}$ form an ellipse with the radius determined by the initial value at t_2.

Similarly, the state trajectory of $T_{{\rm ZVS}2b}$ phase is

$$\left(\frac{i_{\rm Lr}}{I_{\rm pk}} - \frac{C_{2b}}{C_{\rm pj}}\right)^2 + \frac{C_{2b}}{L_rI^2_{\rm pk}}(v_B + v_{\rm pj} - nV_{\rm o})^2 = \left[\frac{i_{\rm Lr}\,(t_3)}{I_{\rm pk}} - \frac{C_{2b}}{C_{\rm pj}}\right]^2 + \frac{C_{2b}v^2_{t3}}{L_rI^2_{\rm pk}}. \tag{38}$$

Finally, the state trajectory of $T_{{\rm ZVS}2c}$ phase is

$$i^2_{\rm Lr} + \frac{C_B}{L_r}\,(v_B - nV_{\rm o})^2 = i^2_{\rm Lr}\,\,(t_4) + \frac{C_B}{L_r}[v_B\,(t_4) - nV_{\rm o}]^2. \tag{39}$$

D. Approximate Estimation of Recovery Factor κ_{rec}

According to (23), dead-time $T_{{\rm ZVS}2a}$ can be approximated as

$$T_{{\rm ZVS}2a} \approx \frac{V_{\rm in}C_A}{I_{\rm pk}}. \tag{40}$$

Consequently, (26) and (28) can be simplified as

$$\begin{cases} v_{\rm pj}\,(t_3) \approx V_{\rm in} + nV_{\rm o} \\ v_{t3} \approx -V_{\rm in}\left(1+\frac{C_A}{C_B}\right) \end{cases}. \tag{41}$$

Since v_A rises to V_{in} at t_3, substituting (25) and (41) into (37), $i_{\text{Lr}}(t_3)$ can be given by

$$\frac{i_{\text{Lr}}(t_3)}{I_{\text{pk}}} = \frac{C_{2a}}{C_{\text{pj}}} - \sqrt{\left(1-\frac{C_{2a}}{C_{\text{pj}}}\right)^2 - \frac{V_{\text{in}}^2 C_{2a}}{I_{\text{pk}}^2 L_r}\left(1+\frac{C_A}{C_B}\right)^2} \approx 1 - \frac{V_{\text{in}}^2 C_A}{2I_{\text{pk}}^2 L_r}\left(1+\frac{C_A}{C_B}\right). \tag{42}$$

Then, as v_{pj} decreases to zero at t_4, substituting (41) and (42) into (38), the elliptic equation about $i_{\text{Lr}}(t_4)$ and $v_B(t_4)$ is

$$\left[\frac{i_{\text{Lr}}(t_4)}{I_{\text{pk}}} - \frac{C_{2b}}{C_{\text{pj}}}\right]^2 + \frac{C_{2b}}{I_{\text{pk}}^2 L_r}\left[v_B(t_4) - nV_{\text{o}}\right]^2 = R^2 \tag{43}$$

where

$$\begin{aligned} R &= \sqrt{\left(\frac{i_{\text{Lr}}(t_3)}{I_{\text{pk}}} - \frac{C_{2b}}{C_{\text{pj}}}\right)^2 + \frac{C_{2b}}{I_{\text{pk}}^2 L_r} v_{t3}^2} \\ &= \sqrt{\left[\frac{C_{\text{pj}}}{C_B + C_{\text{pj}}} - \frac{V_{\text{in}}^2 C_A}{2I_{\text{pk}}^2 L_r}\left(1+\frac{C_A}{C_B}\right)\right]^2 + \frac{V_{\text{in}}^2 C_{2b}}{I_{\text{pk}}^2 L_r}\left(1+\frac{C_A}{C_B}\right)^2} \\ &\approx \frac{V_{\text{in}}}{I_{\text{pk}}}\left(1+\frac{C_A}{C_B}\right)\sqrt{\frac{C_{2b}}{L_r}}. \end{aligned} \tag{44}$$

Combining (44) and the waveforms in Fig. 3(b), $i_{\text{Lr}}(t_4)$ can be approximated as the theoretical minimum

$$\frac{i_{\text{Lr}}(t_4)}{I_{\text{pk}}} \approx \frac{C_{2b}}{C_{\text{pj}}} - R. \tag{45}$$

Besides, the trigonometric functions with respect to $T_{\text{ZVS}2b}$ in (27) can be linearized as

$$\frac{\sin \omega_{2b} T_{\text{ZVS}2b}}{\omega_{2b}} \approx \frac{1-\cos \omega_{2b} T_{\text{ZVS}2b}}{\omega_{2b}} \approx \frac{2}{\pi} T_{\text{ZVS}2b}. \tag{46}$$

Substituting (46) into (27), $T_{\text{ZVS}2b}$ can be approximated as expressed in (47) shown at the bottom of this page. Then substituting (40) and (47) into (30), $v_B(t_4)$ can be approximated as

$$v_B(t_4) \approx \frac{C_A V_{\text{in}} + C_{\text{pj}}\left(\frac{1}{R}-1\right)(V_{\text{in}} + nV_{\text{o}})}{C_B}. \tag{48}$$

Finally, based on (39), (45), and (48), recovery factor κ_{rec} can be estimated in the following equation:

$$\begin{aligned} \kappa_{\text{rec}} &= 1 - \frac{i_{\text{Lr}}^2(t_4)}{I_{\text{pk}}^2} - \frac{C_B}{I_{\text{pk}}^2 L_r}\left[v_B(t_4) - nV_{\text{o}}\right]^2 \\ &= 1 - \left(\frac{C_{2b}}{C_{\text{pj}}} - R\right)^2 \\ &\quad - \frac{\left[C_A V_{\text{in}} + C_{\text{pj}}\left(\frac{1}{R}-1\right)(V_{\text{in}}+nV_{\text{o}}) - C_B n V_{\text{o}}\right]^2}{I_{\text{pk}}^2 L_r C_B}. \end{aligned} \tag{49}$$

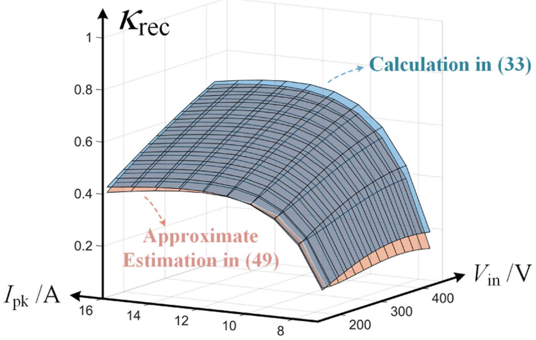

Fig. 9. Comparison between the calculation and the approximate estimation of recovery factor κ_{rec}.

Fig. 9 compares the calculated recovery factor κ_{rec} using (33) with its approximate estimation derived from (49). As shown in Fig. 9, the estimation in (49) closely matches the recovery factor κ_{rec}. Furthermore, qualitative analysis of the estimation method reveals that, lower peak current I_{pk} yields reduced $v_{\text{B}}(t_4)$ based on (48), resulting in an increased $\frac{C_B}{I_{\text{pk}}^2 L_r}[v_B(t_4) - nV_{\text{o}}]^2$ and consequently decreased κ_{rec}. Therefore, achieving the high efficiency secondary-absorption requires careful design of the hardware parameters C_B and C_j, coupled with appropriate limitation of the peak current I_{pk}. The variable-frequency control method in [15] can be implemented to maintain adequate peak current at light load, thereby ensuring sufficient secondary absorption across operational ranges.

IV. ZVS CONDITIONS AND PARAMETER DESIGN

A. *ZVS Conditions of Switches*

Among these switches, soft switching of switch Q_4 can be realized inherently due to the resonance during T_{ZVS3}; the ZVS of switches Q_2, Q_3, and Q_5 can also easily ensured by the minimum peak current constraint; whereas, ZVS of switch Q_1 critically relies on the negative current -I_{neg}, a parameter directly governed by the selection of C_B and C_j. ZVS condition of switch Q_1 can be derived from (2) and (19)

$$V_{\text{in}} < nV_{\text{o}}\sqrt{\frac{C_3}{C_1}}. \tag{50}$$

Considering the maximum input voltage $V_{\text{in,max}}$, the soft-switching requirements for C_B and C_j is given by

$$V_{\text{ZVS}}(C_B, C_j) = nV_{\text{o}}\sqrt{\frac{C_B + C_j/n^2}{C_A + C_j/n^2}} > V_{\text{in,max}}. \tag{51}$$

B. *Design of* $\mathrm{C_B}$ *and* $\mathrm{C_j}$

In each subcell, the selection of each switch is consistent with that in [5], as shown in Table III (see Section III). Once the devices have been determined, output capacitance of each switch

$$T_{\text{ZVS}2b} \approx \frac{V_{\text{in}} + nV_{\text{o}}}{\frac{2}{\pi}\cdot\frac{1}{C_{\text{pj}}}\left[-\frac{C_{\text{pj}}}{C_B+C_{\text{pj}}} I_{\text{pk}} + \frac{V_{\text{in}}^2 C_A}{2I_{\text{pk}} L_r}\left(1+\frac{C_A}{C_B}\right) + V_{\text{in}}\left(1+\frac{C_A}{C_B}\right)\sqrt{\frac{C_{2b}}{L_r}}\right] + \frac{I_{\text{pk}}}{C_B+C_{\text{pj}}}} \approx \frac{C_{\text{pj}}(V_{\text{in}} + nV_{\text{o}})}{V_{\text{in}}\left(1+\frac{C_A}{C_B}\right)\sqrt{\frac{C_{2b}}{L_r}}} \tag{47}$$

TABLE III
KEY COMPONENTS OF THE PROTOTYPE

Components	Model	Components	Model
Switch Q_1	BSC600N25NS3	Switch Q_2	BSZ16DN25NS3
Switch Q_3	BSZ900N15NS3	Switch Q_4	BSC074N15NS5
Switch Q_5	ISZ106N12LM6	Gate driver	ADUM7223
SR driver	NCP4306	Controller	dsPIC33CK64MP102

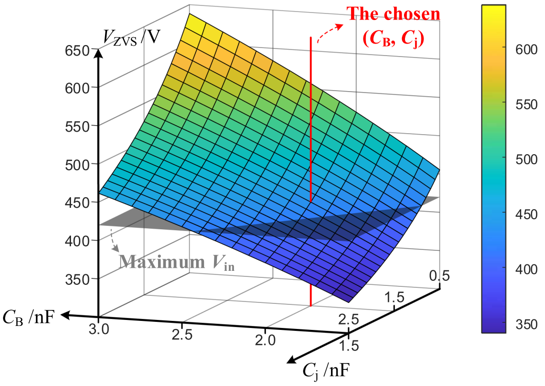

Fig. 10. Curves of V_{ZVS} as function of C_B and C_j.

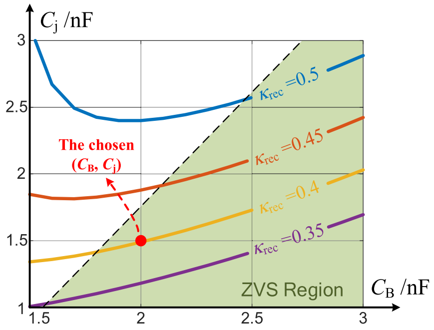

Fig. 11. Design consideration of capacitance C_B and C_j.

can be obtained, and capacitance C_A is about 156 pF, so the appropriate C_B and C_j need to be designed next.

Fig. 10 demonstrates the curves of V_{ZVS} as function of C_B and C_j. Combining Figs. 6 and 10, it can be qualitatively seen that, the design of capacitance C_B and C_j requires a tradeoff of the soft switching performance and secondary absorption ratio. Fig. 11 further shows the relationship between capacitance selection and soft-switching condition in (51), along with the secondary absorption ratio for the minimum input voltage and full load condition, when the peak current peak current reaches its maximum. In addition, as discussed in Section III [5], prolonged dead time would adversely affect power density improvements. As indicated in (20) and (21), dead time T_{ZVS1} and T_{ZVS3} is positively correlated with the capacitance C_B and C_j. Therefore, in order to ensure compliance with soft-switching requirements and a high secondary absorption ratio κ_{rec}, the capacitance C_B and C_j should not be excessively large.

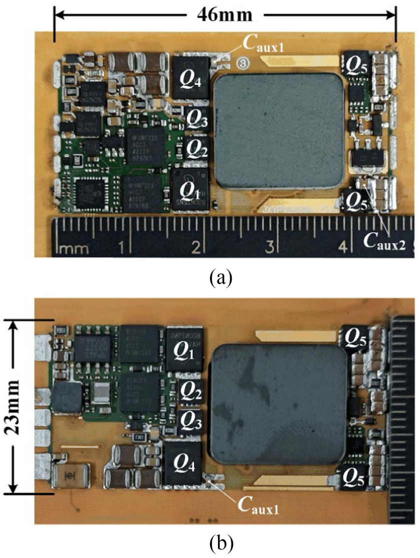

(a)

(b)

Fig. 12. Experimental prototype. (a) Top view. (b) Bottom view.

C. Limit of Peak Current

According to the operating principle of secondary absorption, the resonant current i_{Lr} must remain positive throughout the dead-time T_{ZVS2}. By substituting the condition $i_{\mathrm{Lr}}(t_4) > 0$ into (45), one of the lower bound of the peak current I_{pk} is given by

$$I_{\mathrm{pk}} > V_{\mathrm{in,max}}\left(1+\frac{C_A}{C_B}\right)\left(1+\frac{C_{\mathrm{pj}}}{C_B}\right)\sqrt{\frac{C_{2b}}{L_r}}. \tag{52}$$

Because switch Q_5 is turned ON with soft-switching before switch Q_3, by substituting $v_{\mathrm{B}} < nV_{\mathrm{o}}$ into (48), the upper bound of the peak current I_{pk} is

$$I_{\mathrm{pk}} < V_{\mathrm{in}}\left(1+\frac{C_A}{C_B}\right)\sqrt{\frac{C_{2b}}{L_r}}\left[\frac{C_B nV_{\mathrm{o}} - C_A V_{\mathrm{in}}}{C_{\mathrm{pj}}\left(V_{\mathrm{in}}+nV_{\mathrm{o}}\right)}+1\right]. \tag{53}$$

In addition, by assuming the minimum acceptable recovery factor under light load conditions as κ_{th}, according to (49), another lower bound of the peak current I_{pk} is obtained

$$I_{\mathrm{pk}} > \frac{C_{\mathrm{pj}}\left(V_{\mathrm{in}}+nV_{\mathrm{o}}\right)+C_B nV_{\mathrm{o}} - C_A V_{\mathrm{in}}}{\sqrt{\left(1-\kappa_{\mathrm{th}}\right)L_{\mathrm{r}}C_B}+\frac{C_{\mathrm{pj}}\left(V_{\mathrm{in}}+nV_{\mathrm{o}}\right)}{V_{\mathrm{in}}\left(1+\frac{C_A}{C_B}\right)\sqrt{\frac{C_{2b}}{L_r}}}}. \tag{54}$$

V. EXPERIMENTAL VERIFICATION

A. Experimental Prototype

To verify the proposed secondary absorption scheme for DCZVS flyback converter, a 600-W prototype was fabricated with an input voltage of 160–420 V and an output voltage of 28 V, as shown in Fig. 12. The main parameters of the prototype have been presented in Table II (see Section III), while the component specifications are detailed in Table III. The designed DCZVS prototype consists of switches, drivers, auxiliary power supply, SR, transformer, and controller, with overall dimensions of 46 mm∗23 mm∗7.2 mm. At full load, prototype achieves an ultra-high power density of 1290 W/inch^3.

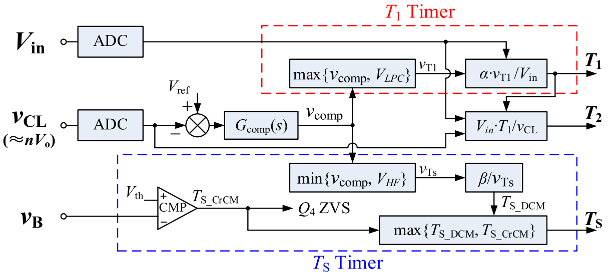

Fig. 13. Variable-frequency multimode PSR control for DCZVS converter.

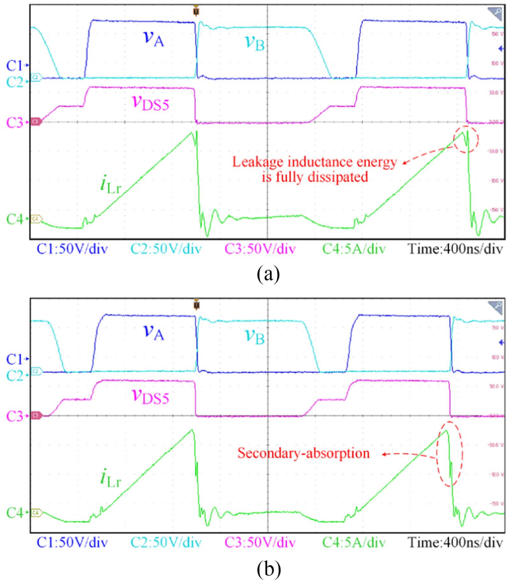

(a)

(b)

Fig. 14. Waveforms tested at 200 V input and 500 W. (a) Without external C_{aux2} ($C_j = 0.5$ nF). (b) With 1 nF external C_{aux2} ($C_j = 1.5$ nF).

As described in Section III, the prototype in this article follows the dual-cell transformer-coupled ISOP structure in [5] with the same low-voltage low figure of merit switches. As shown in Fig. 13, the prototype in this article also adopts the variable-frequency PSR multimode control method for the DCZVS converter in [15], which provides a minimum peak current threshold V_{LPC} at light load.

In addition, the prototype in this article still adopts the 12-layer winding arrangement in [5], and the secondary-side SR driver employs the NCP4306 with the peripheral circuits in [19] for high voltage blocking and power supply. However, it should be noted that, unlike the converter in [5], the prototype in this article discards the series damping resistor of Q_3 and adds an extra capacitor C_{aux2} in parallel with Q_5 to enhance the secondary absorption effect.

B. Steady-State and Transient-State Waveforms

Fig. 14(a) shows the measured waveform of the DCZVS flyback converter without secondary absorption. During T_{ZVS2} phase, the absorption effect of the secondary capacitor is negligible due to the small C_j. The resonant current i_{Lr} recovers to approximately the peak current after a minor dip, indicating that the leakage inductance energy is predominantly dissipated through damping.

In order to verify the secondary absorption scheme, an external 1 nF capacitor C_{aux2} was paralleled to the SR switch to increase C_j. The measured waveform under the same operating condition in Fig. 14(b) exhibits a more pronounced current dip, confirming that the majority of leakage inductance energy is absorbed by the secondary-side capacitance. Furthermore, implementation of the secondary absorption scheme reduces the duration of v_A maintaining a high-level status for the same output power, signifying a shorter energy storage phase T_1 and consequently enabling higher efficiency.

Figs. 15 –17 show the steady-state waveforms of the DCZVS flyback converter with secondary absorption at no-load, half-load (10 A), and full-load (21.5 A) with input voltage V_{in} of 160, 270, and 420 V, respectively. As seen, at light load, peak current I_{pk} remains relatively small, resulting in the less noticeable resonant current dip. With increasing load current, both I_{pk} and the secondary absorption ratio exhibit proportional enhancement, consistent with theoretical predictions. Besides, v_A and v_B waveforms that confirm the successful implementation of soft-switching for all switches, while maintaining essentially constant negative current -I_{neg}.

Fig. 18 shows the transient-state waveforms during load transitions from 10% load to full load at input voltage V_{in} of 160, 270, and 420 V. Due to the PSR implementation where the controller maintains a constant clamp voltage v_{CL} through closed-loop control, minor output voltage v_{o} deviations are observed across different load conditions. The secondary-side absorption scheme enhances PSR precision, limiting output voltage errors within 1.5% across all operational scenarios.

Fig. 19 presents the ZVS waveforms under the most challenging condition of maximum input voltage 420 V, when ZVS of switch Q_1 is most susceptible to failure. As shown in the Q_1 switching sequence, midpoint voltage v_A reaches $\frac{1}{2}V_{\mathrm{in}}$ prior to gate-source voltage v_{gs1} rising, indicating complete discharge of the drain-source voltage v_{DS1} before the channel conducts. Similarly, depending on v_A, v_B and corresponding gate-source voltages, other switches also realize ZVS.

According to the control method illustrated in Fig. 13, the controller turns ON Q_4 exclusively when the comparator detects the v_B reaching zero voltage. This ZVS detection mechanism enables adaptive adjustment of T_{ZVS3}, which aligns with the ZVS waveform in Fig. 19. Besides, the controller incorporates a predefined 100 ns of dead time T_{ZVS1} and T_{ZVS2} between complementary switches in each bridge arm to ensure soft-switching operation. However, experimental results in Fig. 19 indicate that the observed T_{ZVS1} and T_{ZVS2} will be shorter than the predefined 100 ns due to ZVS mechanism. Specifically, body diode initiates current conduction prior to channel conduction, thereby establishing the actual dead time.

C. Performance Analysis

Fig. 20(a)–(c) demonstrates the switching frequency, efficiency performance and output voltage regulation accuracy of

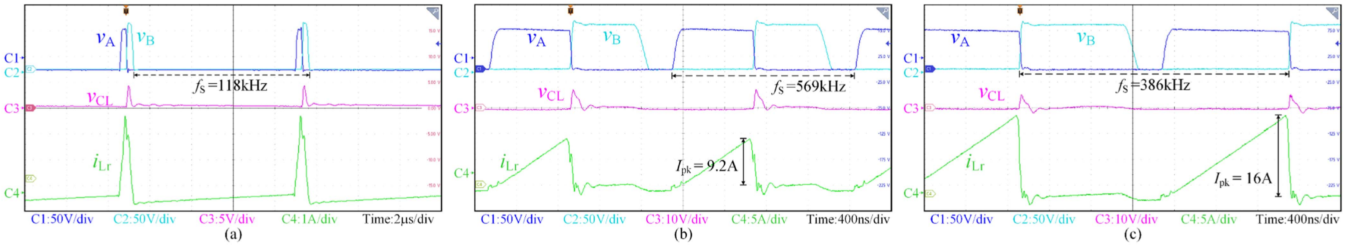

(a) (b) (c)

Fig. 15. Steady-state waveforms at 160 V input. (a) No load condition. (b) Half load condition. (c) Full load condition.

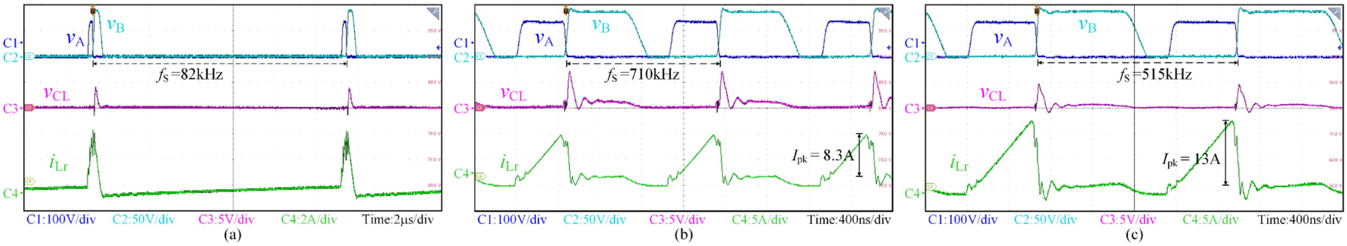

(a) (b) (c)

Fig. 16. Steady-state waveforms at 270 V input. (a) No load condition. (b) Half load condition. (c) Full load condition.

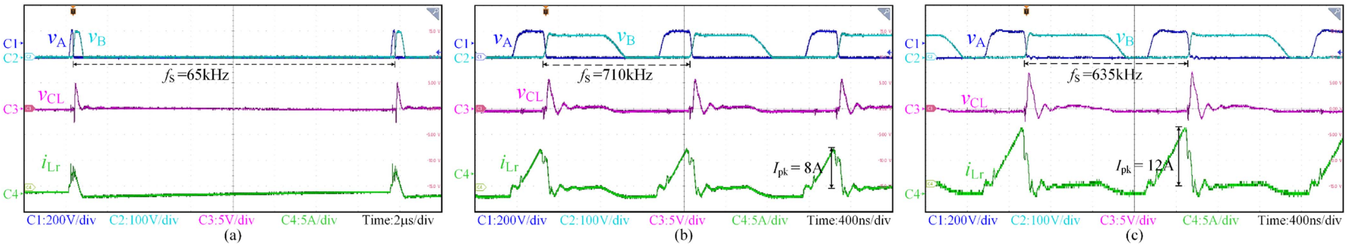

(a) (b) (c)

Fig. 17. Steady-state waveforms at 420 V input. (a) No load condition. (b) Half load condition. (c) Full load condition.

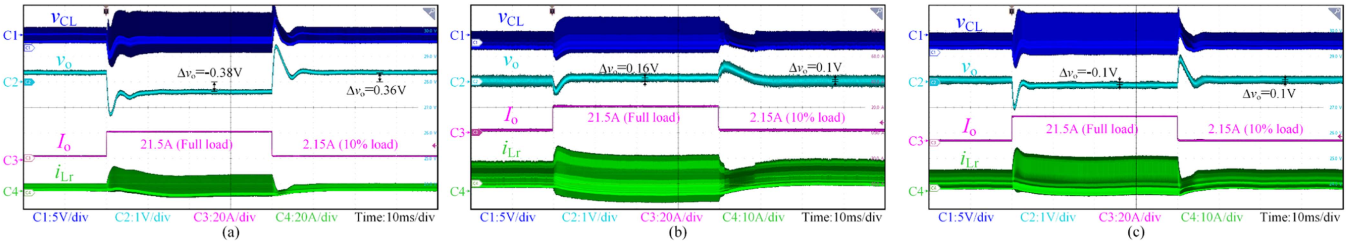

(a) (b) (c)

Fig. 18. Transient-state waveforms from 10% load to 100% load. (a) At 160 V input. (b) At 270 V input. (c) At 420 V input.

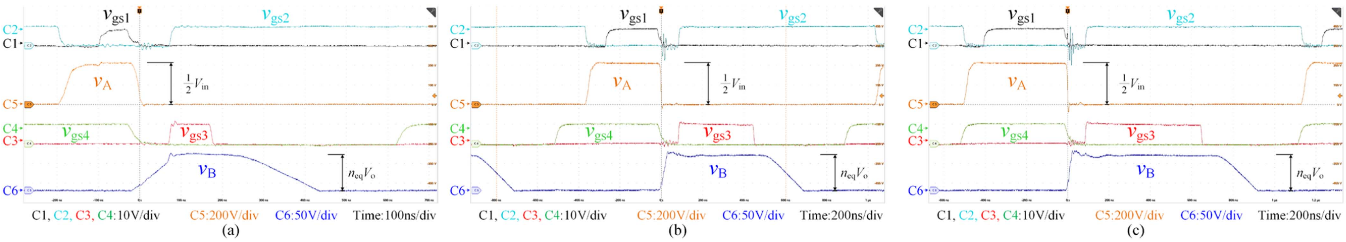

(a) (b) (c)

Fig. 19. Soft switching waveforms at the highest input voltage $V_{\mathrm{in}} = 420$ V. (a) No load condition. (b) Half load condition. (c) Full load condition.

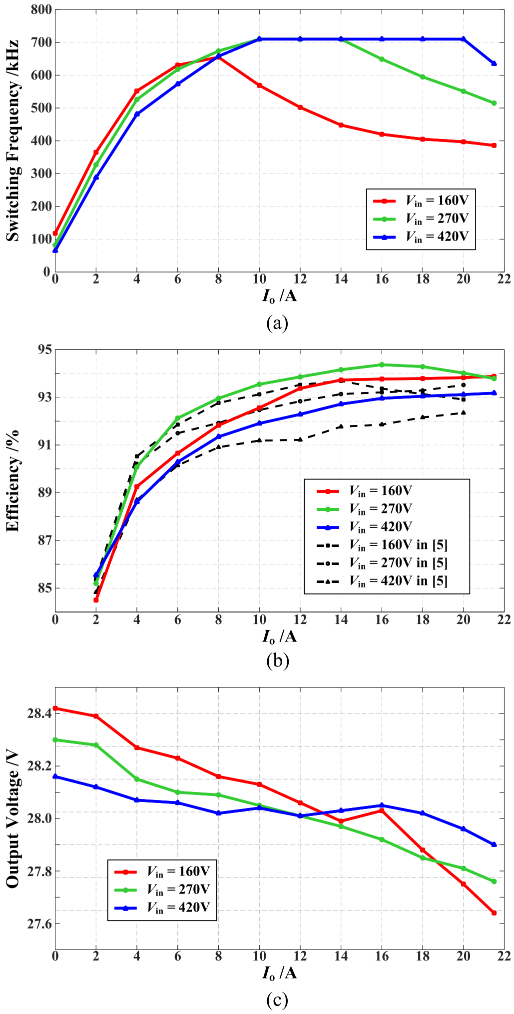

(a)

(b)

(c)

Fig. 20. Prototype performance. (a) Switching frequency. (b) Efficiency. (c) Output voltage accuracy.

the DCZVS flyback prototype under varying loads and input voltages conditions, respectively.

The measured frequency characteristics in Fig. 20(a) align with the variable-frequency multimode control in Fig. 13 [15]. At light load, there is a lower limit on the peak current to ensure the soft switching and secondary absorption, necessitating pulse frequency modulation for voltage regulation with switching frequency increasing proportionally to load current. At heavy load, the converter enters CrCM to maintain a negative current, resulting in an inverse relationship between switching frequency and load current.

The efficiency profile depicted in Fig. 20(b) reveals a peak efficiency is 94.37% at 270 V input with full-load efficiency reaching 93.88%. Comparative analysis with the damping snubber scheme in [5] demonstrates significant efficiency enhancement in heavy-load operation, achieving a 0.68% peak efficiency improvement through a secondary absorption scheme.

Fig. 20(c) illustrates the impact of the secondary absorption scheme on PSR accuracy. The output voltage exhibits a droop characteristic with increasing load due to clamp voltage ripple effects. Compared to the 28V reference voltage, output voltage deviation remains within $+1.5\%$ at no load and -1.3% at full load. The proposed secondary absorption scheme enables high-precision PSR realization in DCZVS flyback converters.

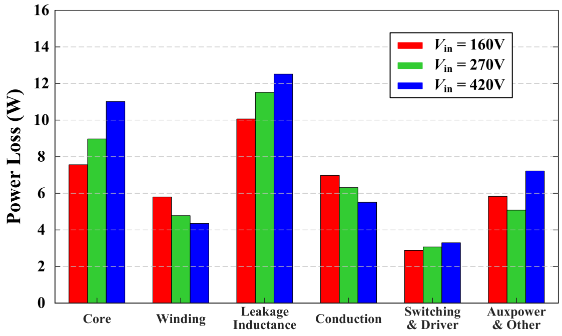

Fig. 21. Full-load loss breakdown.

Fig. 21 shows the full-load loss breakdown calculated from the measured current waveforms. Under full-load operation, transformer loss constitutes the dominant cause of total loss, comprising core loss, winding loss, and leakage inductance loss. The leakage inductance L_r of the transformer is measured to be 4% of the magnetizing inductance L_m, indicating that about 4% of the output power would be dissipated through the damping snubber scheme. In contrast, the secondary absorption scheme substantially reduces leakage inductance loss with a secondary absorption scheme through capacitance C_j. In addition, the elevated core and winding losses primarily result from design constraints imposed by high power density requirements, which necessitate a reduced core area and narrower winding width.

Finally, Table IV summarizes the performances of the proposed secondary absorption scheme for DCZVS flyback converter compared with the state-of-the-art solutions. As outlined in the Introduction, resonance schemes in [9], [10], and [11] require SSR implementation due to significant clamp voltage ripple, necessitating bulky isolation opto-coupler (OC) that compromise power density. The prototype in [5] employs a damping snubbing scheme where leakage inductance energy dissipated through a damping resistor to enable PSR. However, this approach completely wastes the leakage inductance energy, resulting in efficiency degradation. In contrast, the proposed secondary absorption scheme in this article demonstrates two key advantages: it eliminates current-sense resistor $R_{\rm CS}$ and OC to realize inherent high-precision PSR without requiring the auxiliary winding, while simultaneously replacing conventional damping resistor $R_{\rm damp}$ with a secondary-side capacitor that enables partial lossless absorption of leakage inductance energy. The proposed scheme strategy significantly enhances both conversion efficiency and power density through the elimination of dissipative components and recovery of leakage inductance energy. Compared with the previous damping snubbing scheme in [5], which is the highest power density level at present, the experimental prototype achieves a peak efficiency of 94.37% with an increase of 0.68% and achieves an ultra-high power density of 1290 W/inch^3 with an increase of 7.2%. The enhanced power density can be attributed to improved full-load efficiency achieved through the secondary absorption scheme, thereby

TABLE IV
COMPARISON BETWEEN THE SECONDARY ABSORPTION SCHEME FOR DCZVS FLYBACK CONVERTER AND THE STATE-OF-THE-ART

	Vicor [20]	2024 JESTIE [5]	2024 TIE [9]	2024 TPEL [10]	2023 PEAS [11]	This Work
Resonance scheme	N.A.*	Damping snubbing	Resonance absorption	Non-resonant	Non-resonant	Secondary absorption
Control Implementation	N.A.*	PSR	SSR	SSR	SSR	PSR
PSR Accuracy	/	± 1.82%	/	/	/	± 1.5%
Required Components	N.A.*	$C_{\text{aux1}} + R_{\text{damp}}$	$R_{\text{CS}} + C_{\text{aux1}}$ + OC	R_{CS} + OC	OC	$C_{\text{aux1}} + C_{\text{aux2}}$
Input Voltage	160–420 V	160–420 V	80–160 V	200–300 V	36–72 V	160–420 V
Output Voltage	28 V	28 V	12 V	12 V	48 V	28 V
Turns Ratio of Transformer	N.A.*	6	10	24	1	6
Maximum Output Power	500 W	560 W	60 W	400 W	200 W	600 W
Switching Frequency	≤ 720 kHz	100~710 kHz	500 kHz	500 kHz	200 kHz	65~710 kHz
Peak Efficiency	93.9%	93.69%	95.13%	93.46%	94.8%	94.37%
Full load Efficiency	93.2%	93.52%	95.13%	93.24%	94.6%	93.88%
Power Density	1040 W/inch^3	1203 W/inch^3	79 W/inch^3	278 W/inch^3	N.A.*	1290 W/inch^3

N.A.* stands for not available.

enabling greater power output while maintaining equivalent physical dimensions and thermal dissipation capacity.

VI. CONCLUSION

This article proposes a secondary absorption scheme for the DCZVS flyback converter to enhance efficiency and power density. By partially recovering leakage inductance energy through the SR capacitance on the secondary side, the proposed method reduces losses while improving the high-precision PSR characteristics of DCZVS flyback converter. An approximate estimation of the energy recovery ratio, derived from state trajectory analysis during dead-time intervals, is provided to facilitate parameter design. A 600-W prototype was built to demonstrate the benefit of proposed scheme. The DCZVS flyback prototype achieves an ultra-high power density of 1290 W/inch^3 and a peak efficiency of 94.37%, while maintaining ZVS across all switches under all operating condition. The proposed secondary absorption scheme improves efficiency by 0.68% and improves power density by 7.2% over the traditional damping snubbing DCZVS flyback converter. The proposed secondary-absorption scheme significantly improves the efficiency and power density of DCZVS flyback converters, facilitating their applications in aerospace, electric vehicles, and other emerging fields.

REFERENCES

[1] V. Madonna, P. Giangrande, and M. Galea, "Electrical power generation in aircraft: Review, challenges, and opportunities," *IEEE Trans. Transp. Electrific.*, vol. 4, no. 3, pp. 646–659, Sep. 2018.

[2] T. Hong, Z. Geng, K. Qi, X. Zhao, J. Ambrosio, and D. Gu, "A wide range unidirectional isolated DC-DC converter for fuel cell electric vehicles," *IEEE Trans. Ind. Electron.*, vol. 68, no. 7, pp. 5932–5943, Jul. 2021.

[3] Y. Chen, K. Shi, M. Chen, and D. Xu, "Data center power supply systems: From grid edge to point-of-load," *IEEE J. Emerg. Sel. Topics Power Electron.*, vol. 11, no. 3, pp. 2441–2456, Jun. 2023.

[4] M. Salato and P. Kowalyk, "Double-clamp ZVS converter interfaces high voltage traction batteries with 12V legacy system in hybrid and pure-electric vehicles," in *Proc. IEEE Veh. Power Propulsion Conf.*, 2012, pp. 667–670.

[5] S. Ding et al., "High-frequency high-power density multicell transformer-coupled input-series-output-parallel (ISOP) double clamp ZVS flyback converter," *IEEE J. Emerg. Sel. Topics Ind. Electron.*, vol. 6, no. 1, pp. 259–270, Jan. 2025.

[6] P. Vinciarelli, "Double-clamped ZVS buck-boost converter," US Patent 7920391, Apr. 5, 2011.

[7] Q. Liu, S. Ding, T. Wang, and Q. Qian, "A novel multi-mode control method for double-clamped ZVS converter with reduced loss," in *Proc. IEEE Appl. Power Electron. Conf. Expo.*, 2022, pp. 1228–1232.

[8] S. Ding, T. Wang, Q. Liu, Y. Zhou, and Q. Qian, "A novel realization of ZVS and efficiency optimization for double-clamped ZVS buck-boost converter without current sampling," in *Proc. IEEE Appl. Power Electron. Conf. Expo.*, 2022, pp. 743–746.

[9] K. Wang, X. Ruan, T. Fu, F. Liu, and L. Xiao, "A PWM plus voltage-second balance control for ZVS four-switch flyback converter," *IEEE Trans. Ind. Electron.*, vol. 72, no. 3, pp. 2633–2643, Mar. 2025.

[10] T. Fu, X. Ruan, L. Xiao, S. Zhang, and Y. Jiang, "A non-resonant ZVS four-switch flyback converter," *IEEE Trans. Power Electron.*, vol. 39, no. 12, pp. 15915–15923, Dec. 2024.

[11] Y. Li, G. Zhou, and L. Deng, "Power loss minimization control for double-clamped ZVS buck-boost converter," in *Proc. IEEE 2nd Int. Power Electron. Appl. Symp.*, 2023, pp. 1289–1294.

[12] C. Wang, D. Sun, W. Gu, and S. Gui, "Digital voltage sampling scheme for primary-side regulation flyback converter in CCM and DCM modes," *IEEE Trans. Circuits Syst. I: Reg. Papers*, vol. 69, no. 8, pp. 3438–3449, Aug. 2022.

[13] Q. Qian et al., "High precision primary side regulation constant voltage control method for primary and secondary resonant active clamp flyback converter," *IEEE J. Emerg. Sel. Topics Power Electron.*, vol. 10, no. 6, pp. 6985–6999, Dec. 2022.

[14] C.-Y. Tang, W.-Z. Lin, and Y.-C. Tan, "An active clamp flyback converter with high precision primary-side regulation strategy," *IEEE Trans. Power Electron.*, vol. 37, no. 9, pp. 10281–10289, Sep. 2022.

[15] S. Ding, Z. Zhang, L. Chen, Q. Qian, and W. Sun, "Novel sensorless current multimode control for PSR double-clamp ZVS (DCZVS) flyback converter in DCM and CrCM," *IEEE Trans. Circuits Syst. I, Reg. Papers*, vol. 71, no. 9, pp. 4349–4362, Sep. 2024.

[16] L. Xue and J. Zhang, "Highly efficient secondary-resonant active clamp flyback converter," *IEEE Trans. Ind. Electron.*, vol. 65, no. 2, pp. 1235–1243, Feb. 2018.

[17] F. Weiyi and F. C. Lee, "Optimal trajectory control of LLC resonant converters for soft start-up," *IEEE Trans. Power Electron.*, vol. 29, no. 3, pp. 1461–1468, Mar. 2014.

[18] F. Weiyi, F. C. Lee, and P. Mattavelli, "Optimal trajectory control of LLC resonant converters for LED PWM dimming," *IEEE Trans. Power Electron.*, vol. 29, no. 2, pp. 979–987, Feb. 2014.

[19] S. Ding, C. Nie, M. Chen, Z. Zhou, L. Gu, and Q. Qian, "A power supply and high-voltage blocking sensing circuit for high voltage synchronous rectifier," in *Proc. IEEE Appl. Power Electron. Conf. Expo.*, 2024, pp. 679–682.

[20] Vicor, "DCM DC-DC converter," in *DCM4623xD2K31E0y7z Datasheet*. Andover, MA, USA: Vicor Corporation, 2020. [Online]. Available: https://www.vicorpower.com/documents/datasheets/DCM4623xD2K31E0y7z_ds.pdf